Neural Network and Fuzzy Clustering Approach for Automatic Diagnosis of Coronary Artery Disease in Nuclear Medicine

Hassan Bagher-Ebadian, Hamid Soltanian-Zadeh, *Senior Member, IEEE*, Saeed Setayeshi, and Stephen T. Smith

Abstract—We investigated feasibility of using fuzzy clustering and artificial neural network to predict coronary artery disease (CAD) in acute phase from planar and gated SPECT nuclear medicine images. We developed an automatic computerized scheme that helps physicians diagnose coronary artery disease based on 99Tc-Sestamibi myocardial perfusion images. Our study consisted of two separate studies with respect to patient population and imaging method. The first study included 58 subjects (30 male, 28 female) studies using planar rest and stress imaging and a second patient subset of 115 subjects (61 male, 54 female) using gated rest/stress SPECT imaging. After the myocardial perfusion scans, patients also had coronary angiography within three months of the imaging. Signal-to-noise ratio was improved by segmentation of myocardium from its background in both studies using fuzzy clustering with the Picard iteration algorithm. We extracted a set of adaptive features consistent with nature of nuclear medicine imaging and myocardium anatomy. Features were optimized and selected based on maximum separation in multidimensional feature space. A back-propagation artificial neural network (ANN) classifier was trained and tested for each study using the optimal features and the results of coronary angiographies as input and outputs, respectively.

ANNs were trained, optimized, and tested using leave-one-out and Poh's Implementation of Weigned–Rumelhart–Huberman (PIWRH) methods, to diagnose the normal and abnormal patients based on their coronary angiograms. The performances of the optimal ANNs were analyzed by receiver operator characteristic (ROC) method. Results of ANN in the first study were compared to those of the physicians in nuclear medicine ward and two other physicians using ROC method.

Results of ANN for the second study were compared to those of the nuclear medicine ward using ROC method. Both subsets demonstrate that the proposed method outperforms visual diagnosis and is therefore a useful adjunct for CAD diagnosis from planar and gated SPECT images.

Index Terms—Coronary artery disease, feature extraction, fuzzy clustering, image processing, leave-one-out, neural network, nuclear medicine, PIWRH, SPECT.

I. INTRODUCTION

VISUAL interpretation of images in nuclear medicine, even by experienced observers, is subject to substantial variability [1]. Tc^{99m}-Sestamibi myocardial SPECT imaging has been reported to offer major improvements over planar imaging in the detection of coronary artery disease [2]. However, to overcome the difficulties with interpretation of the myocardial SPECT images, a polar-map display, called a bull's-eye image has been developed. Even with this technique, many problems have been described [2]. In addition, the number of experienced radiologists in this field is limited.

The development of a computer-aided diagnostic system or expert system is considered helpful for diagnosis of coronary artery disease (CAD) in nuclear medicine [3]. An expert system (PERFEX) developed for the computer-assisted interpretation of myocardial perfusion SPECT studies is now available. This system uses the bull's-eye map. However, a systematic validation of the diagnostic performance of this expert system for the interpretation of myocardial perfusion SPECT studies has not been reported [4]. PERFEX uses the certainty of the location, size, shape and reversibility of the perfusion defects based on the polar maps and angiography to infer the certainty of the presence and location of CAD [4].

Several researchers have studied CAD recognition with neural networks using bull's-eye maps in nuclear medicine. The bull's-eye maps depend on maximum count in circumferential profiles. However, there is not a one-to-one correspondence between the variation of circumferential counts in the rest and stress images and coronary artery disease. Thus, these maps have significant limitations and prediction of CAD based on bull's-eye may not be appropriate. The operator does three major steps for generating the bull's-eye maps. These steps consist of reconstruction, LV-reorientation and bull's-eye generation. Human error may occur in each step and is propagated through the other steps. These errors may be enhanced in the subsequent steps. Therefore, the quality of bull's-eye maps often depends on the operator's experience and may not be consistent or reproducible.

The purpose of this study is to develop a computerized system; which helps physicians and radiologists to predict the presence of coronary artery disease without using the bull's-eye maps. We use the raw projection data to train a neural network. The neural network is able to analyze the complicated decision-making or pattern-recognition process [3]. The raw data with its complications

TABLE I
PATIENT POPULATION AND DIAGNOSIS OF PHYSICIANS IN NUCLEAR MEDICINE WARD (POSITIVE OR NEGATIVE) WITH RESPECT TO THE PATIENTS' ANGIOGRAMS FOR THE FIRST STUDY

	True-Positive	True-Negative	False-Positive	False-Negative
Male	10 Patients	6 Patients	8 Patient	6 Patients
Female	12 Patients	4 Patients	7 Patient	5 Patients
Total	22 Patients	10 Patients	15 Patients	11 Patients

TABLE II
PATIENT POPULATION AND DIAGNOSIS OF PHYSICIANS IN NUCLEAR MEDICINE WARD (POSITIVE OR NEGATIVE) WITH RESPECT TO THE PATIENTS' ANGIOGRAMS FOR THE SECOND STUDY

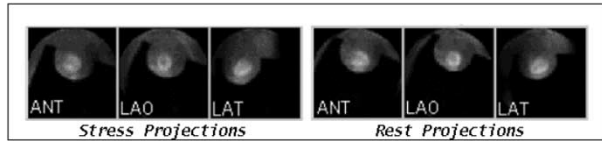|	True-Positive	True-Negative	False-Positive	False-Negative
Male	36 Patients	10 Patients	9 Patient	6 Patients
Female	26 Patients	5 Patients	15 Patient	8 Patients
Total	62 Patients	15 Patients	24 Patients	14 Patients

Fig. 1. Three projections (stress and rest).

relative to the nature of its normal and abnormality was shown to the neural network to make a diagnostic system. Our study consisted of two separate patient populations with different imaging methods (SPECT and planar).

Artificial neural networks learn by example. The number of examples needed for network training depends on the size of the network [5]. A large network fed with many input variables needs many examples to be trained properly [6], [7]. In order to increase the sensitivity of ANN to the input data the images were segmented and the optimal features regarding the myocardium anatomy were extracted. Finally, the performance of trained ANN for each study was compared with expert physicians and nuclear medicine ward using coronary angiographies as gold standard and receiver operator characteristic (ROC) method [8]–[10].

II. MATERIAL AND METHODS

A. Patient Population and Imaging

Our study consisted of two separate groups. The first study included 58 subjects (30 male, 28 female). Patients who during the period from June 1997 to June 1999 had undergone both rest–stress myocardial perfusion planar scan and coronary angiography at Shariati Hospital, Tehran, Iran, were studied retrospectively. The second group consisted 115 patients (61 male, 54 female) patients, who during the period from January 2002 to June 2002 had undergone both rest–stress gated SPECT and coronary angiography at Henry Ford Hospital, Detroit, MI. They are studied retrospectively. The interval between perfusion study and angiography was less than three months in both studies.

1) First Study: As listed in Table I according to the results of patients angiograms, there were 33 abnormal and 25 normal subjects. The ejection fraction was normal in 49 subjects, slightly to moderately reduced in five subjects and severely reduced in four subjects. The data were acquired using planar images in three projections (anterior, left anterior oblique -45 and left lateral) with a 400 mm gamma camera, using a low-energy, general-purpose collimator (FWHM 8.4 mm at 15 cm) and a zoom factor of 1.46 (pixel size 5.45 mm). The size of each image was 64×64. For each patient, images were acquired in two phases (rest and stress) as shown in Fig. 1. Operator used a lead tray to omit the effect of liver superposition in each

projection. Rest and stress studies were performed in a two-day Tc^{99m}-Sestamibi Bruce protocol, using 740 MBq at stress and, after 24 hr, 740 MBq at rest. The period between injection and imaging was 15 min for the stress and 2 hr for the rest study.

In addition, activity decay between the acquired projections was corrected and LEGP collimator correction was applied.

2) Second Study: As shown in Table II, according to the results of patients angiograms, there were 76 abnormal and 39 normal subjects. The SPECT images were acquired using gated method in stress and nongated in rest with a gamma camera circular crystal (ADAC-Vertex), using a low-energy, high-resolution collimator and a zoom factor of 1.46. The size of each image was 64×64. Rest and stress studies were performed in a one-day Tc^{99m}-Sestamibi Bruce protocols, using 25 mCi at stress and, 1 hr using 8 mCi at rest. The period between injection and imaging was 30–45 min for stress and 45–60 min for the rest study. In addition, activity decay between the acquired projections was corrected and LEHR collimator correction was applied.

B. Image Segmentation

The background noise was suppressed by segmenting myocardium form the background using the fuzzy clustering iteration algorithm of Picard [11], [12]. Segmentation in first study was done in three stages and in second study was done in two stages. In each stage, Picard iteration algorithm was used for bi-modal fuzzy clustering. At first, initialization of membership values was random, but in the subsequent stages, the memberships were filled by previous values in order to expedite the convergence. Euclidean distance was used as the distance metric in Picard iteration algorithm [12], [13] but we used the normalized count in each projection for histogram generation.

In the first study, effect of liver superposition was suppressed using a lead tray in each projection. In the second study, the myocardium was segmented from liver using the myocardium temporal motions. In the second study, in order to increase the signal to noise ratio and obtain regular projections the temporal gated SPECT images were added to each other before the segmentation procedure.

C. Feature Extraction

The location of vessels in myocardium varies from patient to patient. Regarding to the nature of cardiac planar and SPECT images and the number of projections obtained, the myocardium was partitioned into four regions (see Table III). During this study, we found that LV orientation has not significant effect to activity distribution for these four regions. As

TABLE III
ANATOMICAL AREA AT THE FOUR REGIONS CORRESPONDING TO THE
PROJECTIONS

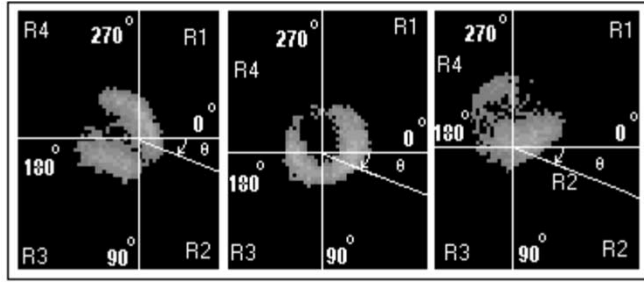| Projection	Region 1	Region 2	Region 3	Region 4
Anterior	Antero-Apical	Apex	Inferior	Base
LAO-45	Antero-Lateral	Infero-Lateral	Infero-Septal	Antero-Septal
Left-Lateral	Infero-Basal	Inferior	Infero-Apical	Anterior

Fig. 2. Three projections and their four regions are shown after fuzzy clustering segmentation.

shown in Fig. 2, the center of activities (*ox,oy*) was calculated for each segmented projection using the following:

$$oy = \bar{Y} = \frac{m_{01}(R_0)}{m_{00}(R_0)}, \quad ox = \bar{X} = \frac{m_{10}(R_0)}{m_{00}(R_0)} \quad (1)$$

$$m_{pq}(R) = \iint_R f(x,y)(x - \bar{X})^p (y - \bar{Y})^q dx\, dy. \quad (2)$$

Circumferential profiles around the center of activity [14], [15] were calculated for each projection. For all projections, the size of radii was fixed to epicardial variation detection. As shown in Fig. 2, direction of sampling was clockwise and the angle interval of each region was 90°. The centers of polar transform for three projections are shown in Fig. 2.

In this study, the extent of radius was 115 mm and the angle was sampled by steps of 2° in the clockwise direction. The six transformed projections (three stress and three rest) are shown in Fig. 3. Two feature vectors were extracted from stress and rest phase of each patient. As shown in Fig. 3, each phase consists of 12 regions and, therefore, feature vectors dimension is 12. We consider he mean and variance row vectors defined by (3)–(6) as our feature vectors. For example, $\vec{\mu}_p = [\mu_p^1, \mu_p^2, \mu_p^3 \cdots \mu_p^{12}]$ denotes the mean vector obtained from phase p (stress or rest). The $\vec{H}_p(i,j)$ points out to the amount of count in position (i,j) in the polar image for phase p. The A_p^m, is obtained by (5) in which $I_p^m(i,j)$ is defined by

$$\mu_p^m = \frac{1}{A_p^m} \sum_i \sum_j H_p^m(i,j), \quad 1 \le m \le 12 \quad (3)$$

$$\Sigma_p^m = \frac{1}{A_p^m} \sum_i \sum_j [H_p^m(i,j) - \mu_p^m]^2, \quad 1 \le m \le 12 \quad (4)$$

$$A_p^m = \sum_i \sum_j I_p^m(i,j) \quad (5)$$

$$I_p^m(i,j) = \begin{cases} 1, & H_p^m(i,j) \ne 0 \\ 0, & H_p^m(i,j) = 0. \end{cases} \quad (6)$$
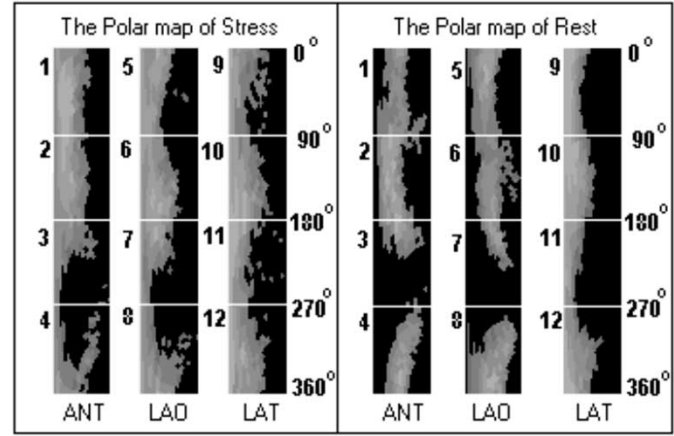

Fig. 3. Three projections in rest and stress phase after polar map transformation are shown.

The CAD was detected by variation of activities between rest and stress phase for all three projections. For this reason, we introduced the following feature vectors:

$$\Delta\vec{\mu} = \vec{\mu}_{\text{Rest}} - \vec{\mu}_{\text{Stress}} \quad (7)$$

$$\Delta\vec{\Sigma} = \vec{\Sigma}_{\text{Rest}} - \vec{\Sigma}_{\text{Stress}}. \quad (8)$$

Each feature vector ($\Delta\vec{\mu}$ or $\Delta\vec{\Sigma}$) consists of 12 elements. For all patients, these feature vectors were extracted from projections [14].

D. Feature Selection

The dimension of feature space obtained from $\Delta\vec{\mu}$ and $\Delta\vec{\Sigma}$ was very large. It is well known that the presence of ineffective features often degrades classifier performance, especially when the training data set is small [15], [16]. Therefore, we selected features (L) based on maximization of Ω_k^L. This function (Ω_k^L) consists of two parts as defined below

$$\Omega_k^L = \sum_{j \in \{L\}} \sum_{p=1}^N \sum_{q=1}^N \frac{|\eta_p^j - \eta_q^j|}{\gamma_p^j + \gamma_q^j}$$

$$+ \sum_{p=1}^N \sum_{i \in \{L\}} \sum_{j \in \{L\}} \frac{|\eta_p^i - \eta_p^j|}{\gamma_p^i + \gamma_p^j} \quad (9)$$

$$k = \binom{M}{L} \quad (10)$$

where the first part, denotes the ratio of the difference in average value of individual features (η_p^j, η_q^j) between the two classes (p, q) to the sum of their variances (γ_p^j, γ_q^j). This quantity will be larger if the selected features have less redundancy (are less similar) between the two classes. The second term, denotes the ratio of the difference in average value of individual classes (η_p^i, η_p^j) between the two features to the sum of their variances (γ_p^i, γ_p^j).

This quantity will be larger if the selected features have larger differences (better discrimination power). In (10), k denotes the number of possibilities for selecting L features from M features. In (9)–(10), L is the number of selected features, M is the number of extracted features, and N is the number of classes ($N = 2, M = 24, L = 12$). For all features, extracted form patients ($n1 = 58, n2 = 115$), the best L features maximizing Ω_k^L,

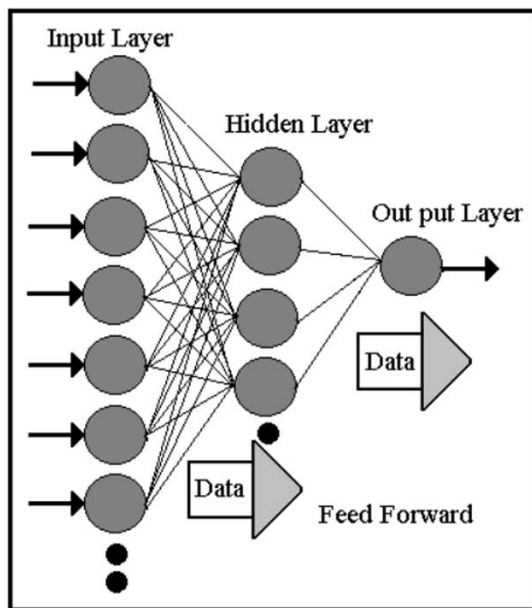Fig. 4.   Artificial neural network architecture.

Fig. 5.   Total sum square error versus epochs for the optimal ANN (13 : 5 : 1). Learning rate: 0.01, Momentum: 0.0.

Fig. 6.   Correct classification fraction versus epoches for study #1 (13 : 5 : 1). Termination error = 0.32. Training and validation: leave-one-out method.

were found. The result showed that the optimal feature vector was the difference vector between the mean vectors obtained at stress and rest, i.e., $\Delta\vec{\mu}$ defined by (7).

E. Artificial Neural Network

We used a feed-forward back-propagation ANN for feature classification in the selected feature space (differences of means). In this ANN, the nodes are organized in the input layer, hidden layers, and the output layer as shown in Fig. 4. The nodes are interconnected by weights and information propagates from one layer to the next through a sigmoid (bi-polar) activation function. Learning rate and momentum factors control the amount of weight adjustment during the training. The learning of the ANN was a supervised process. Detailed description of the back-propagation algorithm can be found in the literature [17], [18]. To improve the convergence rate and the stability of training, we implemented batch processing in which the weight changes obtained from each training case were accumulated and the weights were updated after the entire set of training cases was evaluated. The batch processing method improves the stability with a tradeoff in the convergence rate [19].

We applied two methods, leave-one-out and Poh's implementation of Weigned–Rumelhart–Huberman (PIWRH) [19], [20], for training, testing, and network optimization. In the leave-one-out method, all images of the same patient were left out as test samples in each training cycle and the images from the other (N-1) patients were used for training. The results of all test images from the N training cycles were accumulated to form a test score distribution or correct classification fraction (CCF). This fraction is computed as the ratio of successful classification by the ANN to the total number of samples. In the PIWRH method, images of M patients out of N were selected randomly as a training set and images of N-M patients were left out as test samples. Test results from each cycle were accumulated to form a test score distribution or CCF.
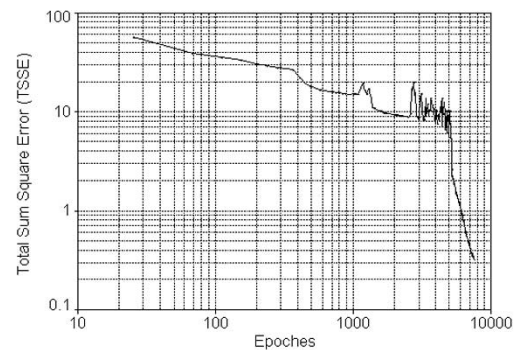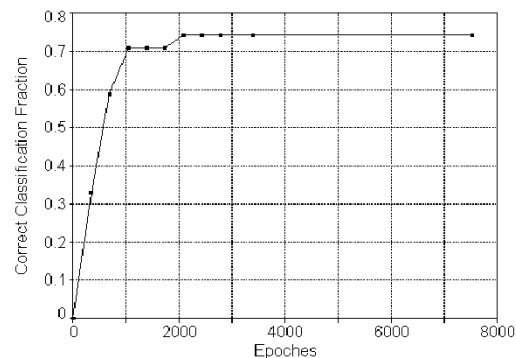
The termination error was selected as the minimum possible error of network for all randomly spilt training sets.

The number of hidden layer nodes may affect the performance of the ANN classifier [21]–[23]. The performance of ANN with respect to the number of hidden layer nodes was examined by considering the ANN responses at preset ANN training termination error levels (leave-one-out: error $= 0.32$ for the first study and error $= 0.36$ for the second study and PIWRH: error $= 0.43$ for the first study and error $= 0.49$ for the second study). Finally, The performance of the optimal ANN classifier was evaluated by ROC methodology [21], [22]. The output value of the ANN was used as the decision variable in the ROC analysis. An ROC curve, which is the relationship between the true-positive fraction (TPF) and false-positive fraction (FPF), is generated by setting different decision thresholds on the output values of the ANNs at the preset training termination error levels as described above. The performances of the optimal ANNs were determined by *Az* test, which is the area under the ROC curve [25].

III. EXPERIMENTAL RESULTS

The ANN classifier was trained and optimized by leave-one-out and PIWRH methods. Fig. 5 shows the typical variation of the total sum square error for ANN as the number of epochs increase. In this example, data are presented for the ANN with 13 : 5 : 1 architecture (optimal) for first study. Typical cumulative scores for correct classification fraction (CCF) shown in Figs. 6–9 indicate that the CCF increases as the number of epochs increases.

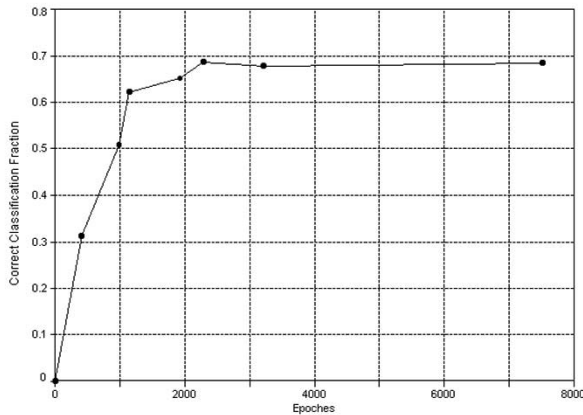The training and optimization were repeated for the ANN with different number of nodes in the hidden layer. In each

Fig. 7.   Correct classification fraction versus epoches for study #1 (13 : 5 : 1). Termination error $= 0.43$. Training and validation: PIWRH method.
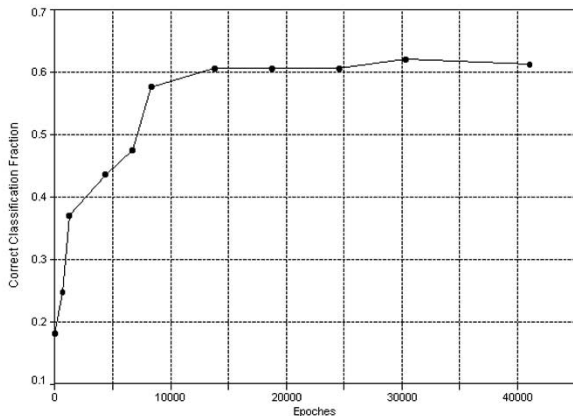

Fig. 8.   Correct classification fraction versus epoches for study #2 (13 : 7 : 5 : 1). Termination error $= 0.36$. Training and validation: leave-one-out method.
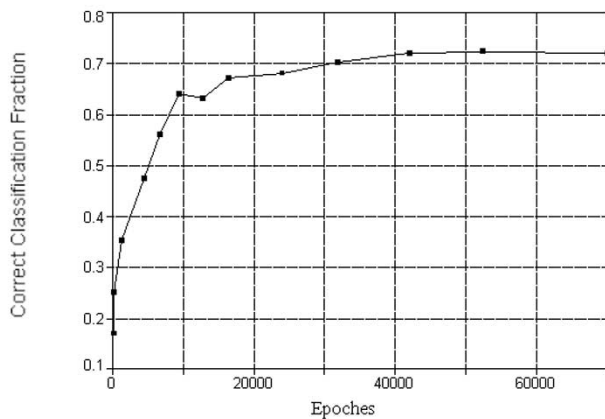

Fig. 9.   Correct classification fraction versus epoches for study #2 (13 : 7 : 5 : 1). Termination error $= 0.49$. Training and validation: PIWRH method.

case, the final CCF at the termination error level (leave-one-out: error level $= 0.32$ for the first study and error $= 0.36$ for the second study and PIWRH: error $= 0.43$ for the first study and error $= 0.49$ for the second study) was determined [21], [23]. The ANN structure with maximum CCF value was considered as the optimal network in each study and each method.
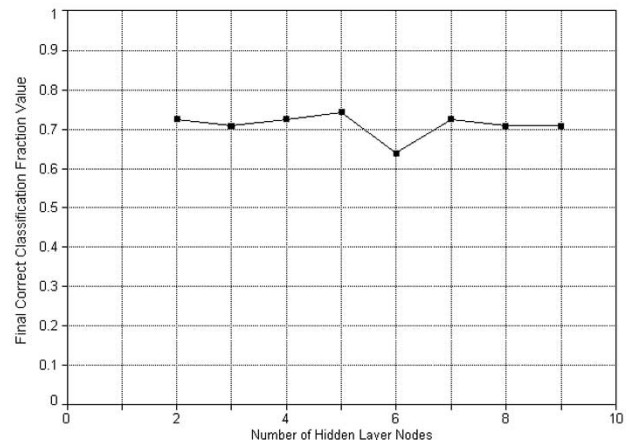

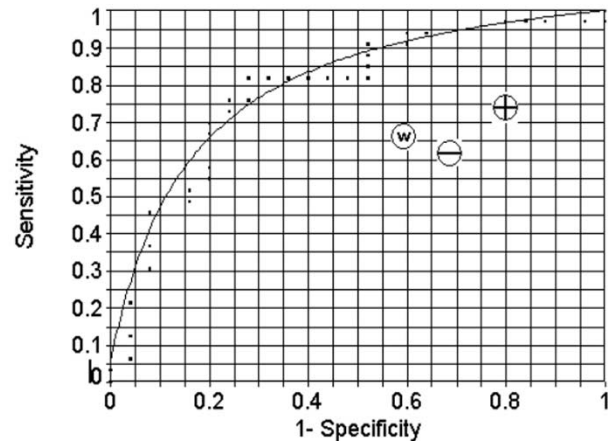Fig. 10.   Hidden layer nodes optimization using final correct classification value for study #1.

Fig. 11.   Receiver operator characteristic curve for the optimal ANN (13 : 5 : 1, TSSE $= 0.32$, leave-one-out method), with points representing the physician's performance for first study. (w) Nuclear medicine ward: TPF: 0.66, FPF: 0.60 ($+$) expert (physician) no. 1: TPF: 0.75, FPF: 0.80 ($-$) expert (physician) no. 2: TPF: 0.60, FPF: 0.68.

As shown in Fig. 10, the optimal number of nodes in the hidden layer was five for the first study. We had two hidden layers with seven and five nodes, respectively, in the second study. In the leave-one-out method the CCF values were 0.74 for the first study and 0.68 for the second study. In the PIWRH method the CCF values were 0.69 for the first study and 0.61 for the second study. The ROC curves were generated for these optimal architectures (13:5:1 for the first study and 13 : 7 : 5 : 1 for the second study). The ROCs, i.e., graphs of sensitivity (true positive fraction) versus 1-specificity (false positive fraction) are shown in Figs. 11–14 for the first and the second study, respectively. The results obtained from two physicians and the nuclear medicine ward at Shariati hospital, Tehran, Iran, also are shown on Figs. 11 and 12. The results obtained from the nuclear medicine ward at Henry Ford Hospital, Detroit, MI, also are shown in Figs. 13 and 14. The overall performance of the optimal ANNs (the first study, 13 : 5 : 1 and error $= 0.32$ and 0.43 for leave-one-out and PIWRH and the second study, 13 : 7 : 5 : 1 and error $= 0.36$ and 0.49 for leave-one-out and PIWRH) were determined as the integral under the ROC curve, which were 0.80 and 0.77 for the first and second studies, respectively, using
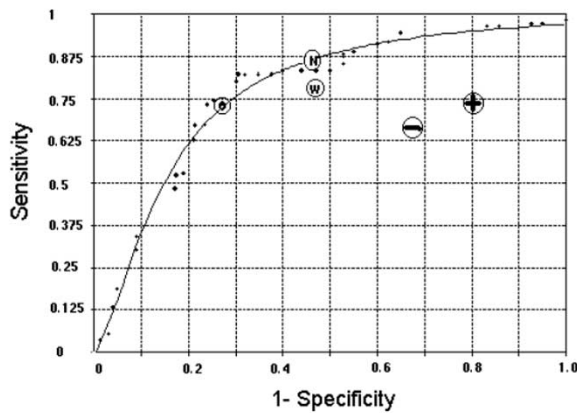
Fig. 12. Receiver operator characteristic curve for the optimal ANN $(13:5:1,$ $\mathrm{TSSE} = 0.43$, PIWRH method), with points representing the physicians performance for first study. (w) Nuclear medicine ward: TPF: 0.66, FPF: 0.60 $(+)$ expert (physician) no. 1: TPF: 0.75, FPF: 0.80 $(-)$ expert (physician) no. 2: TPF: 0.60, FPF: 0.68.
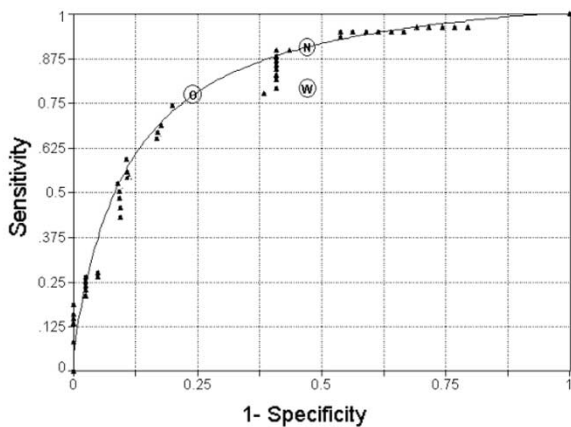

Fig. 13. Receiver operator characteristic curve for the optimal ANN $(13:7:5:1,$ $\mathrm{TSSE} = 0.36$, leave-one-out method), with points representing The ward performance for second study (w) nuclear medicine ward: TPF: 0.81, FPF: 0.62 (N) ANN ward: TPF: 0.91, FPF: 0.62 (O) optimal ANN: TPF: 0.77, FPF: 0.76.

the leave-one-out method, and were 0.77 and 0.73, respectively, using the PIWRH method. Amounts of positive predictive value (PPV) and negative predictive value (NPV) at the prevalence of 0.54 for the first study and 0.66 for the second study were also estimated using the population of 58 and 115 patients, respectively. In addition, NPV and PPV for an optimal threshold, which is found as the intersection of the ROC curve with the line of sensitivity $=$ specificity were computed. Tables IV–VII compare the values of PPV and NPV for the two physicians, the nuclear medicine ward, and the ANNs for both studies [31]. These tables clearly illustrate superiority of the ANNs compared to the visual inspection of the images by the physicians in both studies.

IV. DISCUSSION

Our attempt to apply neural network for CAD detection in nuclear medicine has been quite successful in acute phase of myocardial infarction. The ANNs proved to be capable of extracting essential characteristics from noisy images and
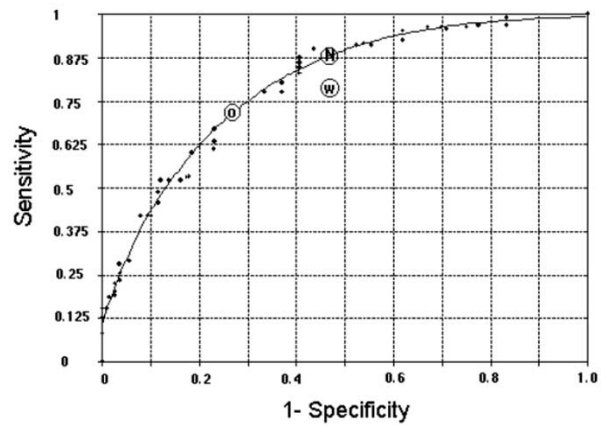
Fig. 14. Receiver operator characteristic curve for the optimal ANN $(13:7:5:1,$ $\mathrm{TSSE} = 0.49$, PIWRH method), with points representing the ward performance for second study (w) nuclear medicine ward: TPF: 0.81, FPF: 0.62 (N) ANN ward: TPF: 0.87, FPF: 0.62 (O) optimal ANN: TPF: 0.74, FPF: 0.72.

TABLE IV
POSITIVE PREDICTION VALUES AND NEGATIVE PREDICTION VALUES FOR DIGNOSIS OF THE NUCLEAR MEDICINE WARD, EXPERT #1, EXPERT #2, AND THE OPTIMAL ANN (LEAVE-ONE-OUT) AT THE PREVALENCE OF 0.568 ARE SHOWN WITH THEIR CORRESPONDING SPECIFICITIES AND SENSITIVITIES FOR THE FIRST STUDY

	SPECIFICITY	SENSITIVITY	PPV	NPV
WARD	0.40	0.66	59%	60%
ANN –WARD	0.40	0.85	71%	73%
EXPERT#1	0.20	0.75	55%	70%
ANN-EXPERT#1	0.20	0.95	64%	75%
EXPERT#2	0.32	0.60	54%	53%
ANN-EXPERT#2	0.32	0.91	63%	73%
ANN-OPTIMUM	0.72	0.73	77%	66%

TABLE V
POSITIVE PREDICTION VALUES AND NEGATIVE PREDICTION VALUES FOR DIAGNOSIS OF THE NUCLEAR MEDICINE WARD, EXPERT #1, EXPERT #2, AND THE OPTIMAL ANN (PIWRH METHOD) AT THE PREVALENCE OF 0.568 ARE SHOWN WITH THEIR CORRESPONDING SPECIFICITIES AND SENSITIVITIES FOR THE FIRST STUDY

	SPECIFICITY	SENSITIVITY	PPV	NPV
WARD	0.40	0.66	59%	60%
ANN –WARD	0.54	0.85	71%	73%
EXPERT#1	0.20	0.75	55%	70%
ANN-EXPERT#1	0.20	0.95	64%	75%
EXPERT#2	0.32	0.60	54%	53%
ANN-EXPERT#2	0.32	0.91	63%	73%
ANN-OPTIMUM	0.72	0.73	77%	66%

TABLE VI
POSITIVE PREDICTION VALUES AND NEGATIVE PREDICTION VALUES FOR DIGNOSIS OF THE NUCLEAR MEDICINE WARD AND THE OPTIMAL ANN (LEAVE-ONE-OUT) AT THE PREVALENCE OF 0.66 ARE SHOWN WITH THEIR CORRESPONDING SPECIFICITIES AND SENSITIVITIES FOR THE SECOND STUDY

	SPECIFICITY	SENSITIVITY	PPV	NPV
WARD	0.38	0.81	72%	51%
ANN –WARD	0.38	0.91	95%	80%
ANN-OPTIMUM	0.76	0.77	86%	63%

learning from angiograms. The recognition performances of the optimal ANNs are superior to that of the experienced physicians (see Figs. 11, 12, and Tables IV–VII). As shown in Tables IV and V the ANNs detect CAD in myocardial images more accurately than the expert physicians and nuclear medicine ward. The proposed approach is more appropriate than the optimal detection theory because the complexity of

TABLE VII
POSITIVE PREDICTION VALUES AND NEGATIVE PREDICTION VALUES FOR
DIAGNOSIS OF THE NUCLEAR MEDICINE WARD AND THE OPTIMAL
ANN (PIWRH) AT THE PREVALENCE OF 0.66 ARE SHOWN WITH THEIR
CORRESPONDING SPECIFICITIES AND SENSITIVITIES FOR THE SECOND STUDY

	SPECIFICITY	SENSITIVITY	PPV	NPV
WARD	0.38	0.81	72%	51%
ANN −WARD	0.38	0.92	74%	70%
ANN-OPTIMUM	0.74	0.71	84%	57%

anatomical structures and noise for nuclear medicine images makes the estimation of probability density functions of the two classes of images extremely difficult. There are differences between the CCF values and integrals of the ROC curves for the two different methods (leave-one-out and PIWRH). This difference is justifiable because the training set in the PIWRH method was significantly smaller than that of the leave-one-out method (almost 35%).

The SPECT images are constructed from series of planar images with major properties of LV-orientation and liver superposition. It is impossible to omit the effect of liver superposition from the SPECT images during the data acquisition and the LV-orientation may vary from patient to patient. In the second study (SPECT), the three projections were selected automatically by the program so the essential features may vary due to these variations. In addition, anatomical registration between projection series (stress and rest) may vary from patient to patient. This study showed that the ANNs are powerful in adapting with these data variations. Determining the amount and location of coronary artery stenosis, clearly needs more clinical and technical information. Limited accuracy of coronary angiography and myocardial SPECT for predicting the site of subsequent acute myocardium infarction (MI) are reported by some researchers [26]–[28].

They have shown that stress myocardial perfusion scintigraphy fails to detect nonflow-limiting mild coronary stenosis. Correlation between the location of a SPECT defect, the most severe coronary stenosis, and the location of a subsequent AMI (acute myocardium infarction) and concordance between SPECT and coronary angiography to identify the most severe defects are investigated by other researchers [29]. However, considering the results presented in the literature, it can be concluded that prediction of disease (CAD) versus no-disease (no-CAD) from the perfusion study is more reliable than prediction of CAD location, site and amount of stenosis. Therefore, in this study, we concentrated on prediction of CAD versus no-CAD instead of the site and amount of stenosis. Our task was prediction of CAD in acute time for mild, moderate, and severe cases from planar and SPECT perfusion images.

We proposed the CAD recognition using projection images. In the first study, the effect of liver was omitted by the operator in each spot using a lead tray. In addition, the effect of LV-orientation was omitted by selecting the desired projection. In the second study (SPECT), the temporal motion helps to suppress the effect of liver and the ANN was adapted to variation of LV orientation. In addition, in the second study (SPECT) the projections could be selected by manual or semi-automated methods [31].

In this paper, we used three projections to design the ANN and evaluate its performance. It is well known that the performance of human observers in detecting lesions from a limited number of projections is inferior to that using three-dimensional (3-D) activity distributions. A major point of this paper has been to show that the ANN works well even with three projections. The results have been compared to those of the human observers seeing all of the 3-D images. Still, the ANN performed the physicians (see Figs. 11–14).

We used datasets from the same equipment to train and test the proposed ANN, which is the customary approach in the field. The performance of the ANN may degrade if data from different equipment and imaging parameters are used in the training and testing. We followed the general approach of using "different" datasets for training and testing. For a comprehensive evaluation, we used two training and testing methods (leave-one-out and PIWRH). The PIWRH method does not have the limitation of the leave-one-out method in possible over-estimation of the ANN performance.

We used clinically available data that incorporate no correction for scatter and attenuation, but include correction for variable collimator response. To the best of our knowledge, there are no well-accepted and routinely used methods for scatter and attenuation corrections. There are disagreements between researchers and nuclear medicine physicians in using the existing methods, because some believe that applying these methods may increase the chance of diagnostic artifacts. Note that a significance of the proposed methods is that, as the results show, they work on the uncorrected images. They may even work better on the corrected images, but because of the reasons stated above, we did not apply any correction methods. This can be considered in the future as widely accepted correction methods become available.

The size of the patient, the activity distribution in the patient, and the distance between the heart and the collimator may affect delectability of myocardial lesions. These effects are inherent in the datasets we used in our studies, because we have not excluded any specific dataset from the study (the datasets were selected randomly). Also, we have used the patient studies from two different institutions during two different time intervals.

The proposed method deals with the basic aspects for pre-diagnosis of either CAD or no-CAD in nuclear medicine images and it can be adapted for the analysis of SPECT images to create an ideal observer. By ideal observer, we mean a neural-network-assisted system to help physicians improve their diagnosis. Accurate determination of the location and amount of the disease using the techniques presented in this paper may be considered as a direction for future work. Another direction can be finding the optimal set of myocardium segments that are more sensitive compared to the other sets for detection of CAD. This optimization can be done for offset location and number of projections.

APPENDIX A

The fuzzy clustering algorithm provides possible solutions to accommodate the structural details in segmented description, since it identifies each of the clusters as a fuzzy set characterized by a membership distribution. A fuzzy set $\mathbf{A}$ is characterized by a membership function $\mu_A(x) \in [0, 1]$, which provides compatibility or attachment of $\mathbf{x}$ to $\mathbf{A}$. The problem of

fuzzy clustering is that of partitioning the set of **n** sample points $X = \{x_1, x_2, x_3, \ldots x_n\}$ into **c** classes such that the membership distribution has the following properties:

$$\mu_i(x_j) \in [0, 1] \tag{1}$$

$$0 < \sum_{j=1}^{n} \mu_i(x_j) < n \tag{2}$$

$$\sum_{j=1}^{n} \mu_i(x_j) = 1.0. \tag{3}$$

Objective function-based algorithms have been largely used for the identification of fuzzy partitions. The fuzzy c-means algorithm, minimizes a least square objective function

$$J = \sum_{i=1}^{cn} \sum_{j=1}^{n} \mu_i(x_j)^\tau d(x_j, v_i)^2 \tag{4}$$

to generate c hyper-spherical clusters. If j denotes gray level, in (4), $d(x, v)$ is considered as the Euclidean distance in one dimension between v_i and j. The parameter $\tau \geq 1$ controls the amount of fuzziness in the partition and when $\tau = 1$, the minima of (4) provides an equivalent classification as the k-means algorithm.

Let $\{h_j\}$ be the histogram and $\{p_j\}$ be the probability distribution associated with the gray values (**L**) of the image to be thresholded and $j \in \{0, 1, \ldots, L-1\}$. Thresholding may be formulated by modifying (4) with c = 2 as

$$J = \sum_{i=1}^{2} \sum_{j=1}^{L-1} h_j \mu_i(x_j)^p d(x_j, v_i)^2. \tag{5}$$

The clusters' means for the classes, i.e.,

$$v_i = \frac{\sum_{j=0}^{L-1} j h_j \mu_i(j)^\tau}{\sum_{j=0}^{L-1} h_j \mu_i(j)^\tau}, \quad i = 1, 2 \tag{6}$$

characterize the background and object regions. The objective function (5) can be iteratively minimized by computing the means using (6) and updating the memberships as

$$\mu_o(j) = \frac{1}{1 + [d(j, v_o)/d(j, v_B)]^{\frac{2}{\tau-1}}} \tag{7}$$

and

$$\mu_O(j) = 1 - \mu_B(j) \tag{8}$$

where $\mu_O(j)$ and denote object and background membership functions respectively. The fuzzy thresholding algorithm can be formally stated as follows.

1) Initialize the threshold description $\mu_O(j)$ and $\mu_B(j)$ satisfying (1)–(3).
2) Compute the mean gray values of both regions using (6).
3) Assign the membership values using (7).
4) Repeat Steps 2–4 until there is no appreciable change for $\mu_O(j)$ and $\mu_B(j)$.

Even though the fuzzy c-means algorithm is a generalization of the hard k-means algorithm, its properties associated with the thresholded description-based on the above algorithm are quite different from the k-means algorithm. An **L** gray value image can be represented by a set of **L** real values in threshold description and reflect the geometry associated with the gray distribution. At the same time, the fuzzy thresholded description is more general, Since a hard threshold equivalent to the one obtained from k-means, can be obtained from fuzzy thresholded description [11].

REFERENCES

[1] G. B. Trobaugh, F. J. T. Wackeres, E. B. Sokole, T. A. Derouen, J. L. Ritchi, and G. W. Hamilton, "Thallium-201 myocardial imaging: An interinstitial study of observer variability," *J. Nucl. Med.*, vol. 19, pp. 359–363, 1978.
[2] M. J. Guiberteau, *Nuclear Cardiovascular Imaging: Current Clinical Practice*. New York: Churchill Livingston, 1990.
[3] F. Hiroshi and K. Tetsuro, "Neural network approach for computer-aided diagnosis of coronary artery diseases in nuclear medicine," in *Proc. 1992 Int. Joint Conf. Neural Networks (IJCNN'92)*, vol. III, Balitmore, MD, June 7–11, 1992, pp. 215–220.
[4] E. V. Garcia, C. D. Cooke, R. D. Folks, C. A. Santana, E. G. De, L. Braal, and N. F. Ezquerra, "Diagnostic performance of an expert system for the interpretation of myocardial perfusion SPECT studies," *J. Nucl. Med.*, vol. 42, no. 8, pp. 1185–1191, 2001.
[5] D. Lindahi, J. palmer, M. Ohlsson, C. Peterson, A. Lundin, and L. Edenbrandt, "Automated interpretation of myocardial SPECT perfusion images using artificial neural networks," *J. Nucl. Med.*, vol. 38, no. 12, pp. 1870–1875, Dec. 1997.
[6] G. D. Tourassi, C. E. Floyd, H. D. Sostman, and R. E. Coleman, "Artificial neural network for diagnosis of acute pulmonary embolisme: Effect of case and observer selection of radiology," *J. Nucl. Med.*, vol. 194, pp. 889–893, 1995.
[7] H. Fujita, T. Katafuchi, T. Uehara, and T. Nishimura, "Application of artificial neural network to computer-aided diagnosis of coronary artery disease in myocardial spect bull's-eye images," *J. Nucl. Med.*, vol. 33, pp. 272–276, 1992.
[8] J. Krzysztof, S. Lucy, K. Kanu, and S. Gursel, "A novel algorithm for classification of SPECT images of a human heart," in *Proc. 9th IEEE Symp. Computer-Based Medical Systems Symp.*, Ann Arbor, MI, June 14–17, 1996, Univ. Michigan, pp. 1–5.
[9] D. Cianflone, O. Carandente, M. Carlino, C. Meloni, and S. L. Chierchia, "Efficient performance of neural network models as artificial intelligence prediction tools in cardiology," *Comput. Cardiol.*, vol. 1, pp. 599–601, 1991.
[10] D. Georgia, B. S. Tourassi, E. Carey, J. R. Floyd, M. T. Munley, J. E. Bowsher, and R. E. Coleman, "Application of neural network to lesion detection in SPECT," *IEEE Trans. Nucl. Sci.*, vol. 3, pp. 2179–2183, 1991.
[11] C. V. Jawahar and P. K. Biswas, "Investigation on fuzzy thresholding based on fuzzy clustering," *Pattern Recogn.*, vol. 41, no. 10, pp. 1605–1613, 1997.
[12] C. V. Jawahar and A. K. Ray, "Incorporation of gray level imprecision in representation and processing of digital images," *Pattern Recogn.*, vol. 17, pp. 541–546, 1996.
[13] A. B. D. Boudraa, M. Arzi, J. Sau, J. Champier, S. H. Moussa, J. E. Besson, D. S. Marinier, R. Itti, and J. J. Mallet, "Automated detection of the left ventricular region in gated nuclear cardiac imaging," *IEEE Trans. Biomed. Eng.*, vol. 43, pp. 430–436, Apr. 1996.

[14] X. S. Liao and M. Pawlak, "On image analysis by moments," *IEEE Trans. Pattern Anal. Machine Intell.*, vol. 18, pp. 254–266, Mar. 1996.

[15] K. Fukunaga and R. Hayes, "Effects of sample size on classifier design," *IEEE Trans. Pattern Anal. Machine Intell.*, vol. 11, pp. 873–885, June 1989.

[16] S. Raudy and V. Pickelis, "On dimensionality, sample size, classification, error and complexity of classification algorithm in pattern recognition," *IEEE Trans. Pattern Anal. Machine Intell.*, vol. PAMI-2, pp. 242–252, 1980.

[17] J. Freeman and D. Skapura, *Neural Network-Algorithms, Applications and Programming Techniques*. Reading, MA: Addison-Wesley, 1991.

[18] H. Chan, B. Sahiner, N. Petrick, M. A. Helvie, K. L. Lam, D. D. Alder, and M. M. Goodsitt, "Computrized classification of malignant and benign microcalsification on mammograms: Texture analysis using an artificial neural network," *Phys. Med. Biol.*, vol. 42, pp. 549–567, 1996.

[19] H. L. Poh, "A Neural Network Approach for Marketing Strategies Research and Decision Support," Ph.D. dissertation, Stanford Univ., Stanford, CA, 1991.

[20] C. G. Looney, *Pattern Recognition Using Neural Networks Theory and Algorithms for Engineers and Scientists*. New York: Oxford Univ. Press, 1997.

[21] M. E. Ashrafi, H. Bagher-Ebadian, and E. Yahaghi, "Pre-optimization of radiotherapy treatment planning: An artificial neural network calssification aided technique," *Phys. Med. Biol.*, vol. 44, no. 6, pp. 1513–1528, June 1999.

[22] S. J. Sheppard, E. L. Hines, D. Taylor, and J. Barham, "Diagnosis of single photon emission tomography images using artificial neural networks," *Med. Imaging*, vol. 3, pp. 1–3, 1992.

[23] S. Jang, R. J. Jaszczak, B. M. W. Tsui, C. E. Metz, D. R. Gilland, T. G. Turkington, and R. E. Coleman, "ROC evaluation of SPECT myocardial lesion detectability with and without nonuniform attenuation compensation using an anthropomorphic femal phantom," *IEEE Trans. Nucl. Sci.*, vol. 45, pp. 2080–2088, 1998.

[24] L. Patino, L. Mertz, E. Hirsch, B. Dumitresco, and A. Constantinesco, "Contouring blood pool myocardial gated SPECT images with a neural network leader segmentation and a decision-based fuzzy logic," in *Proc. IEEE Fuzzy Systems*, vol. 2, Barcelona, Catalonia, Spain, July 1–5, 1997, pp. 969–974.

[25] M. John, V. G. Sigillito, and G. S. Shaber, "Neural networks in radiology: An introduction and evaluation in a signal detection task," *Med. Phys.*, vol. 17, pp. 234–241, 1990.

[26] W. C. Little, M. Constantinescu, and R. J. Applegate, "Can coronary angiography predict the site of a subsequent myocardial infarction in patients with mild-to-moderate coronary artery disease?," *Circulat.*, vol. 78, pp. 1157–1166, 1988.

[27] J. M. Galvin and K. A. Brown, "The site of acute myocardial infarction is related to the coronary territory of transient defects on prior myocardial perfusion imaging," *J. Nucl. Cardiol.*, vol. 3, pp. 382–388, 1996.

[28] G. L. Miller, S. D. Herman, and G. V. Heller, "Relation between perfusion defects on stress technetium-99 m sesta-MIBI SPECT scintigraphy and the location of a subsequent acute myocardial infarction," *Amer. J. Cardiol.*, vol. 78, pp. 26–30, 1996.

[29] J. Candell-Riera, O. Pereztol-Valdes, C. Santana-Boado, M. Missorici, G. Oller-Martinez, S. Aguade-Bruix, J. Castell-Conesa, M. Simo, M. J. Diez-Castro, and J. Soler-Soler, "Relationship between the location of the most severe myocardial perfusion defects, the most severe coronary artery stenosis, and the site of subsequent myocardial infarction," *J. Nucl. Med.*, vol. 42, no. 4, pp. 558–563, Apr. 2001.

[30] L. R. Goldfarb, R. C. Goldfarb, and D. W. Seldin, "Clinical decision making in nuclear medicine," in *Nuclear Medicine Annual 1989*. New York: Raven Press, pp. 225–264.

[31] H. Bagher-Ebadian, H. Soltanian-Zadeh, and S. Setayeshi, "Neural network approach to diagnose of coronary artery disease in nuclear medicine," in *Proc. 4th Irano-Armenian Workshop Neural Network*, Tehran, Iran, May 2002, pp. 27–34.